Article

Bipolar outflows out to 10 kpc for massive galaxies at redshift $z \approx 1$

Yucheng Guo[1✉], Roland Bacon[1], Nicolas F. Bouché[1], Lutz Wisotzki[2], Joop Schaye[3], Jérémy Blaizot[1], Anne Verhamme[4], Sebastiano Cantalupo[5], Leindert A. Boogaard[6], Jarle Brinchmann[3,7], Maxime Cherrey[1], Haruka Kusakabe[4,8], Ivanna Langan[1,9], Floriane Leclercq[10], Jorryt Matthee[11], Léo Michel-Dansac[1], Ilane Schroetter[12] & Martin Wendt[13]

Galactic outflows are believed to play a critical role in the evolution of galaxies by regulating their mass build-up and star formation[1]. Theoretical models assume bipolar shapes for the outflows that extend well into the circumgalactic medium (CGM), up to tens of kiloparsecs (kpc) perpendicular to the galaxies. They have been directly observed in the local Universe in several individual galaxies, for example, around the Milky Way and M82 (refs. 2,3). At higher redshifts, cosmological simulations of galaxy formation predict an increase in the frequency and efficiency of galactic outflows owing to the increasing star-formation activity[4]. Galactic outflows are usually of low gas density and low surface brightness and therefore difficult to observe in emission towards high redshifts. Here we present an ultra-deep Multi-Unit Spectroscopic Explorer (MUSE) image of the mean Mg II emission surrounding a sample of galaxies at $z \approx 1$ that strongly suggests the presence of outflowing gas on physical scales of more than 10 kpc. We find a strong dependence of the detected signal on the inclination of the central galaxy, with edge-on galaxies clearly showing enhanced Mg II emission along the minor axis, whereas face-on galaxies show much weaker and more isotropic emission. We interpret these findings as supporting the idea that outflows typically have a bipolar cone geometry perpendicular to the galactic disk. We demonstrate that this CGM-scale outflow is prevalent among galaxies with stellar mass $M_* \gtrsim 10^{9.5} M_\odot$.

During the past ten years, integral field spectrograph facilities such as the Very Large Telescope (VLT)/MUSE (ref. 5) and the Keck/Keck Cosmic Web Imager (KCWI) (ref. 6) have enabled mapping the CGM in emission using several tracers, such as Lyα (refs. 7–12), C IV, He II and C III (ref. 13), and other rest-frame optical emission lines[14,15]. Yet Lyα emission can only be observed by ground-based facilities at $z \gtrsim 2$ and, owing to the severe effects of cosmological surface-brightness dimming, it is very difficult to obtain spatially resolved spectroscopy at such high redshifts.

The Mg II $\lambda\lambda2796,2803$ doublet presents a potential alternative to Lyα for tracing the CGM. Owing to its resonant nature, extended Mg II emission is expected to occur under similar conditions as Lyα. The ionization potential of Mg I (7.6 eV) is lower than that of H I (13.6 eV), implying that the CGM remains at least partly neutral when Mg II is produced. This makes Mg II a more promising tracer of the cool and metal-enriched CGM gas compared with Lyα. The line can be observed from the ground at redshifts $z \gtrsim 0.1$ (ref. 16), facilitating higher linear resolution and much lower surface-brightness dimming. Nevertheless, the detection of circumgalactic Mg II is challenging because Mg II is

intrinsically much fainter than Lyα. So far, extended Mg II emission was detected around two galaxies by long-slit spectra[17,18] and also more recently by integral field spectrographs (refs. 19–21). The occurrence frequency and outflow nature of the extended Mg II emission are still unclear and, therefore, we do not know if it is a common feature of galaxies across the mass spectrum.

We answer this question using extremely deep MUSE observations of a sample of galaxies at $z \approx 1$ in the Hubble Ultra Deep Field[22]. We use Hubble Space Telescope (HST) images to construct a sample of 112 edge-on and 60 face-on galaxies. We perform an oriented stacking of the MUSE datacube segments after aligning each edge-on galaxy along the direction of the photometric major axis. We stack the face-on galaxies by their original sky orientations. Before stacking, we remove the continuum and mask bright neighbouring objects in each individual datacube (Methods).

We then construct Mg II $\lambda2796$ pseudo-narrowband (NB) images by summing the stacked datacubes in the spectral direction, followed by spatial filtering. Figure 1 shows the stacking results of the HST images (stellar component) and of the Mg II $\lambda2,796$ line emission. We clearly

[1]Univ Lyon, Univ Lyon1, Ens de Lyon, CNRS, Centre de Recherche Astrophysique de Lyon UMR5574, Saint-Genis-Laval, France. [2]Leibniz-Institut für Astrophysik Potsdam (AIP), Potsdam, Germany. [3]Leiden Observatory, Leiden University, Leiden, The Netherlands. [4]Observatoire de Genève, Université de Genève, Versoix, Switzerland. [5]Dipartimento di Fisica "G. Occhialini", Università degli Studi di Milano Bicocca, Milano, Italy. [6]Max Planck Institute for Astronomy, Heidelberg, Germany. [7]Instituto de Astrofísica e Ciências do Espaço, Centro de Astrofísica da Universidade do Porto (CAUP), Porto, Portugal. [8]National Astronomical Observatory of Japan (NAOJ), Mitaka, Tokyo, Japan. [9]European Southern Observatory, Garching, Germany. [10]Department of Astronomy, The University of Texas at Austin, Austin, TX, USA. [11]Department of Physics, ETH Zürich, Zürich, Switzerland. [12]Institut de Recherche en Astrophysique et Planétologie, Université Toulouse III - Paul Sabatier, CNRS, CNES, Toulouse Cedex 04, France. [13]Institut für Physik und Astronomie, Universität Potsdam, Golm, Germany. ✉e-mail: yucheng.guo@univ-lyon1.fr

Article
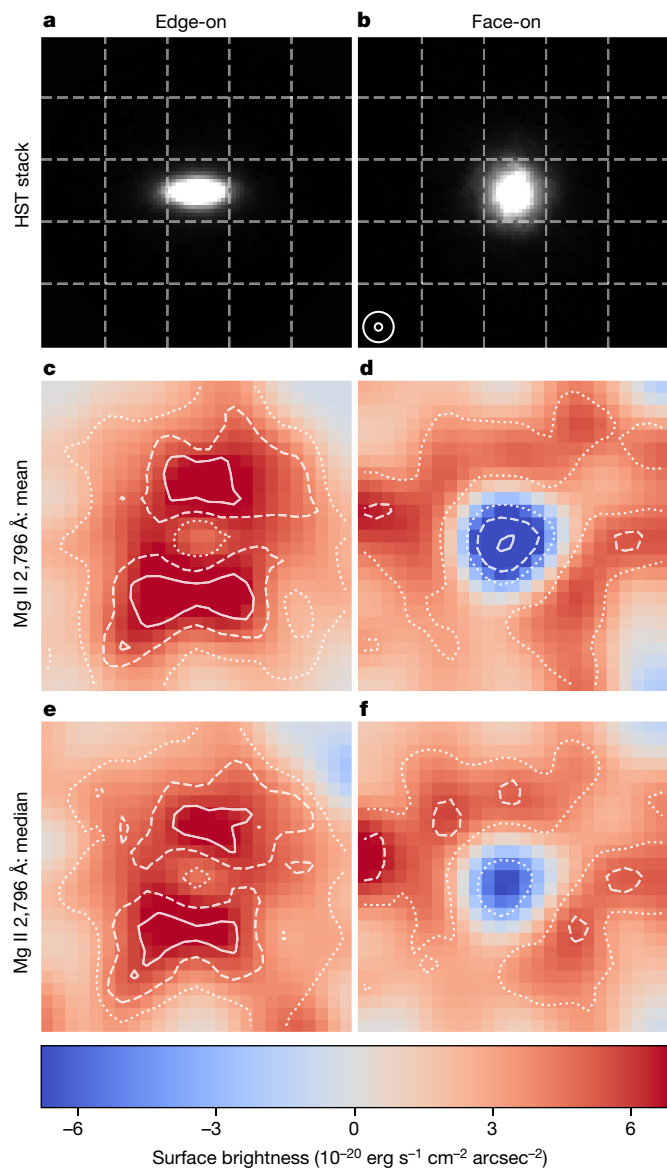
Fig. 1 | The stacked stellar continuum and Mg II emission. a,b, The stacked average of HST images (F435W, F775W, F606W, F850LP and F160W bands), representing the stellar component. **c–f,** The mean (**c,d**) and median (**e,f**) stacked Mg II 2,796 Å pseudo-NB images, smoothed by a Gaussian kernel of width 0.4″. The white contours correspond to Mg II significance levels of 2σ, 4σ and 6σ (dotted, dashed and solid lines, respectively). Each thumbnail has a size of 5″ × 5″, corresponding to about 40 × 40 kpc at the median redshift of the sample. Each grid cell in **a** and **b** corresponds to a distance of about 8 kpc. The smaller and larger circles in **b** represent the PSF full width at half maximum of the HST and the MUSE, respectively. We extract spectra from each grid cell shown in **a** and **b** and present them in the corresponding panels in Extended Data Fig. 5.

detect resolved Mg II emission extending over CGM scales. The scale of each thumbnail is 5″ × 5″ (corresponding to about 40 × 40 kpc at the median redshift of the sample).

The stack of edge-on galaxies in the left column of Fig. 1 shows a clear enhancement of Mg II emission along the minor axis. We detect a bipolar shape extending out to a radius of about 10 kpc in the stacked cube, suggesting that this is because of gas recently ejected from the galaxy. This anisotropic emission is seen in both the mean and median stacked cubes, indicating that the Mg II outflows are common among our galaxy sample. We verify that this anisotropic pattern does not result from a few bright outliers but is a generic property of galaxies in our sample (Methods).

We do not detect strong extended emission around the face-on galaxies. There is, however, strong Mg II absorption in the central region coinciding with the stellar component of the galaxies. In the outer region, we see a weak ring pattern in both the mean and median stacks. The detection of the ring is robust (Methods). The physical origin for this pattern is unclear. It might be attributed to an isotropic Mg II halo, to inflowing or reaccreted gas or to a face-on outflow cone extending to even larger radii. Further observations and simulations are needed for a better understanding.

To visualize the kinematic structure of the extended Mg II emission, we split the wavelength range of the NB image of Fig. 1 into three velocity intervals of 100 km s^{-1}, shown in Fig. 2. For edge-on galaxies, the anisotropic Mg II emission is seen in all velocity intervals, although it is less evident in the bluest channel. At the velocity centred on the systemic velocity, we detect strong emission both above and below the galaxy disk. Towards positive velocities, at which there is no longer central absorption, Mg II is still strong along the minor axis. This shows that the anisotropic Mg II emission is an inherent property of the CGM and independent of the central absorption of the stellar component of the galaxy. The face-on sample shows central absorption at all velocity intervals. It is strongest in the most negative velocity range and gets successively weaker towards redder wavelengths. At all velocities, the central absorption is stronger for face-on galaxies than for edge-on systems.

To study the stellar-mass dependence of the Mg II emission, we split our sample into halves around the median mass of the sample, $10^{9.5} M_\odot$. As shown in Fig. 3, only the high-mass edge-on subsample shows the anisotropic Mg II emission. The corresponding high-mass face-on subset, in contrast, shows very strong central absorption surrounded by a noisy emission-ring-like feature. On the other hand, the low-mass subsample does not show such anisotropic emission, with both the edge-on and the face-on orientations presenting emission of irregular morphology. This could hint at a more irregular geometry of outflows in the low-mass systems. However, as a caveat, we note that low-mass galaxies are smaller, implying that the impact of the point spread function (PSF) is more pronounced, so that smaller-scale wind signatures would be more difficult to detect. A correlation between galaxy Mg II equivalent width and stellar mass was previously reported[23,24], in which the Mg II emitters generally have lower masses than Mg II absorbers, with a transition occurring around $10^{9.5} M_\odot$.

In Fig. 4, we compare the spectra extracted from the central regions of the high-mass galaxies. Evidently, the Mg II absorption profile of the face-on galaxies is much broader than that of the edge-on galaxies. If we assume that the two samples of galaxies have similar properties except for their inclination, then the widening of the absorption line indicates the typical velocity of the outflow (v_{out}). We use two independent methods to measure this velocity, obtaining a consistent estimate of $v_{out} \approx 180$ km s^{-1} (Methods).

Galactic outflows are responsible for removing potential fuel for star formation from the galaxy while, at the same time, enriching the CGM and the intergalactic medium. These feedback processes, although incorporated as key elements of cosmological simulations, are still poorly constrained on CGM scales. Recent observations find that the Mg II $\lambda\lambda 2796,2803$ absorption occurs preferentially close to the major or minor axes of the galaxies[25,26]. It is particularly strong along the minor axis, at which the metal-enriched outflows are expected[27,28]. However, direct imaging observations of such outflows, as well as the frequency of their occurrence, are largely missing. In this study, we discover that the anisotropic Mg II emission extending up to approximately 10 kpc is common for massive ($M_* \gtrsim 10^{9.5} M_\odot$) edge-on galaxies at $z \approx 1$. This finding provides the most direct evidence of the prevalence of cool and metal-enriched galactic outflows at high redshift. Simulations predict that most of the metals produced inside high-redshift galaxies are carried out by galactic winds[29]. The galactic winds may produce an anisotropic metallicity distribution in the CGM (ref. 30). The results of
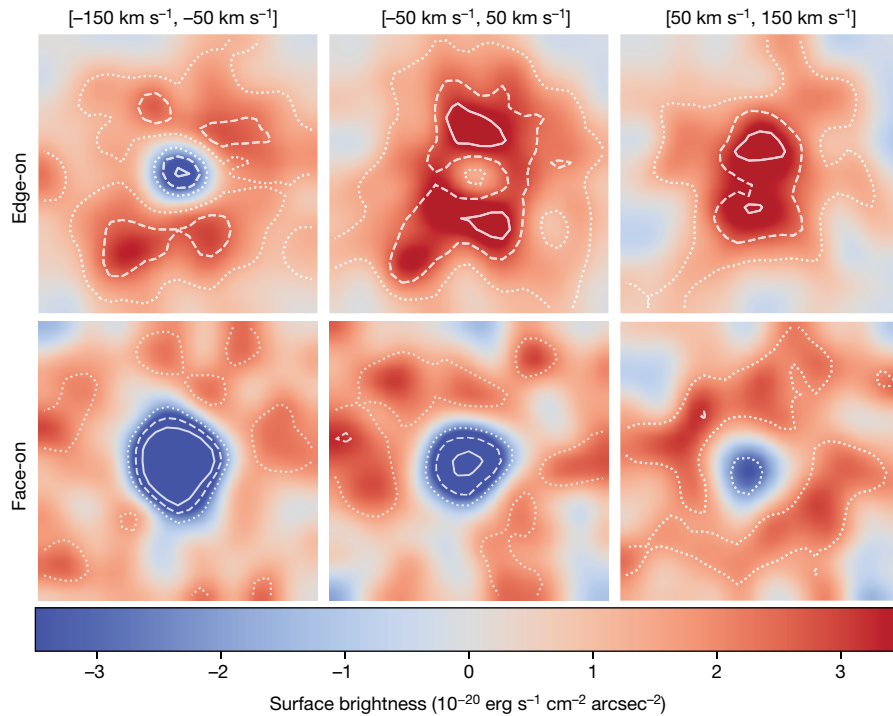
Fig. 2 | Pseudo-NB images for different velocity bins. The images are extracted in intervals of 100 km s^{-1} (≈1 Å in the rest frame) centred at Mg II 2,796 Å, then smoothed by a Gaussian of width 0.4″. The upper and lower rows show the edge-on and face-on samples, respectively. The white contours correspond to Mg II significance levels of 2σ, 4σ and 6σ (dotted, dashed and solid lines, respectively). All scales and annotations are as in Fig. 1.

this paper provide further support for the key role of galactic winds in the transport of metals from the galaxy to the CGM.

Online content

Any methods, additional references, Nature Portfolio reporting summaries, source data, extended data, supplementary information, acknowledgements, peer review information; details of author contributions and competing interests; and statements of data and code availability are available at https://doi.org/10.1038/s41586-023-06718-w.

1. Tumlinson, J., Peeples, M. S. & Werk, J. K. The circumgalactic medium. *Annu. Rev. Astron. Astrophys.* **55**, 389–432 (2017).
2. Predehl, P. et al. Detection of large-scale X-ray bubbles in the Milky Way halo. *Nature* **588**, 227–231 (2020).
3. Bland, J. & Tully, B. Large-scale bipolar wind in M82. *Nature* **334**, 43–45 (1988).
4. Muratov, A. L. et al. Gusty, gaseous flows of FIRE: galactic winds in cosmological simulations with explicit stellar feedback. *Mon. Not. R. Astron. Soc.* **454**, 2691–2713 (2015).
5. Bacon, R. et al. The MUSE second-generation VLT instrument. *Proc. SPIE* **7735**, 773508 (2010).
6. Morrissey, P. et al. The Keck Cosmic Web Imager integral field spectrograph. *Astrophys. J.* **864**, 93 (2018).
7. Wisotzki, L. et al. Extended Lyman α haloes around individual high-redshift galaxies revealed by MUSE. *Astron. Astrophys.* **587**, A98 (2016).
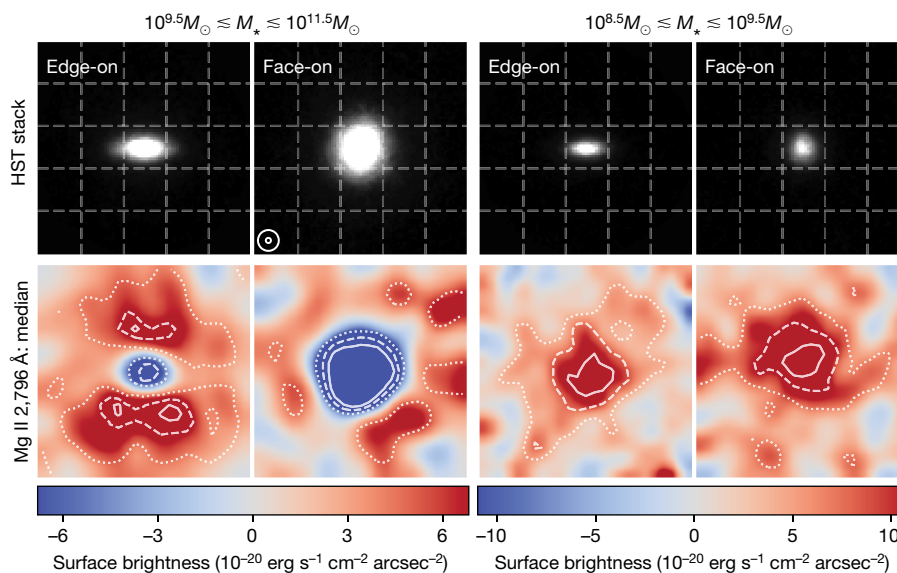
Fig. 3 | Comparison of the high-mass and low-mass subsamples. The subsamples are bisected at the median stellar mass of 10$^{9.5}$$M_\odot$. The colour scales were adjusted for presentation purposes. The white contours correspond to Mg II significance levels of 2σ, 4σ and 6σ (dotted, dashed and solid lines, respectively). All scales and annotations are as in Fig. 1.

Article
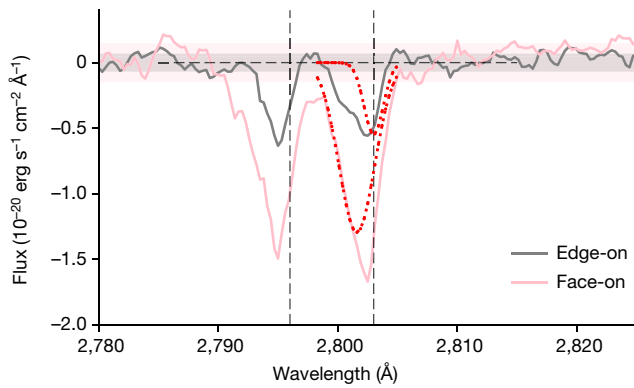
Fig. 4 | Continuum-subtracted mean spectra of the high-mass galaxies. The spectra are extracted from the central 1″. The pink and grey spectra show the face-on and edge-on galaxy subsamples, respectively. The dotted red lines present the double-Gaussian decomposition of the Mg II 2,803 Å line (Methods). The two vertical dashed lines denote the wavelengths of the Mg II doublet. The horizontal dashed line denotes the zero-flux level. The shading represents the 1σ error ranges of the corresponding spectra. The EWs of the Mg II 2,796 Å line for the face-on and edge-on galaxy subsamples are 7.4 ± 0.9 Å and 2.5 ± 0.7 Å, respectively.

8. Wisotzki, L. et al. Nearly all the sky is covered by Lyman-α emission around high-redshift galaxies. *Nature* **562**, 229–232 (2018).
9. Leclercq, F. et al. The MUSE Hubble Ultra Deep Field Survey. VIII. Extended Lyman-α haloes around high-z star-forming galaxies. *Astron. Astrophys.* **608**, A8 (2017).
10. Cai, Z. et al. Evolution of the cool gas in the circumgalactic medium of massive halos: a Keck Cosmic Web Imager survey of Lyα emission around QSOs at z ≈ 2. *Astrophys. J. Suppl. Ser.* **245**, 23 (2019).
11. Kusakabe, H. et al. The MUSE eXtremely Deep Field: individual detections of Lyα haloes around rest-frame UV-selected galaxies at z ≃ 2.9–4.4. *Astron. Astrophys.* **660**, A44 (2022).
12. Bacon, R. et al. The MUSE Extremely Deep Field: the cosmic web in emission at high redshift. *Astron. Astrophys.* **647**, A107 (2021).
13. Guo, Y. et al. Metal enrichment in the circumgalactic medium and Lyα halos around quasars at z ~ 3. *Astrophys. J.* **898**, 26 (2020).
14. Johnson, S. D. et al. Directly tracing cool filamentary accretion over >100 kpc into the interstellar medium of a quasar host at z = 1. *Astrophys. J. Lett.* **940**, L40 (2022).
15. Herenz, E. C. et al. A ~15 kpc outflow cone piercing through the halo of the blue compact metal-poor galaxy SBS0335−052E. *Astron. Astrophys.* **670**, A121 (2023).
16. Kacprzak, G. G., Cooke, J., Churchill, C. W., Ryan-Weber, E. V. & Nielsen, N. M. The smooth Mg II gas distribution through the interstellar/extra-planar/halo interface. *Astrophys. J. Lett.* **777**, L11 (2013).
17. Rubin, K. H. R. et al. Low-ionization line emission from a starburst galaxy: a new probe of a galactic-scale outflow. *Astrophys. J.* **728**, 55 (2011).
18. Martin, C. L. et al. Scattered emission from z ~ 1 galactic outflows. *Astrophys. J.* **770**, 41 (2013).
19. Burchett, J. N. et al. Circumgalactic Mg II emission from an isotropic starburst galaxy outflow mapped by KCWI. *Astrophys. J.* **909**, 151 (2021).
20. Zabl, J. et al. MusE GAs FLOw and Wind (MEGAFLOW) VIII. Discovery of a MgII emission halo probed by a quasar sightline. *Mon. Not. R. Astron. Soc.* **507**, 4294–4315 (2021).
21. Leclercq, F. et al. The MUSE eXtremely deep field: first panoramic view of an Mg II emitting intragroup medium. *Astron. Astrophys.* **663**, A11 (2022).
22. Bacon, R. et al. The MUSE Hubble Ultra Deep Field surveys: data release II. *Astron. Astrophys.* **670**, A4 (2023).
23. Kornei, K. A. et al. The properties and prevalence of galactic outflows at z ~ 1 in the Extended Groth Strip. *Astrophys. J.* **758**, 135 (2012).
24. Feltre, A. et al. The MUSE Hubble Ultra Deep Field Survey. XII. Mg II emission and absorption in star-forming galaxies. *Astron. Astrophys.* **617**, A62 (2018).
25. Bouché, N. et al. Physical properties of galactic winds using background quasars. *Mon. Not. R. Astron. Soc.* **426**, 801–815 (2012).
26. Zabl, J. et al. MusE GAs FLOw and Wind (MEGAFLOW) II. A study of gas accretion around z ≈ 1 star-forming galaxies with background quasars. *Mon. Not. R. Astron. Soc.* **485**, 1961–1980 (2019).
27. Martin, C. L., Ho, S. H., Kacprzak, G. G. & Churchill, C. W. Kinematics of circumgalactic gas: feeding galaxies and feedback. *Astrophys. J.* **878**, 84 (2019).
28. Schroetter, I. et al. MusE GAs FLOw and Wind (MEGAFLOW) – III. Galactic wind properties using background quasars. *Mon. Not. R. Astron. Soc.* **490**, 4368–4381 (2019).
29. Muratov, A. L. et al. Metal flows of the circumgalactic medium, and the metal budget in galactic haloes. *Mon. Not. R. Astron. Soc.* **468**, 4170–4188 (2017).
30. Péroux, C. et al. Predictions for the angular dependence of gas mass flow rate and metallicity in the circumgalactic medium. *Mon. Not. R. Astron. Soc.* **499**, 2462–2473 (2020).

Methods

Data reduction and analysis
This work is mainly based on data release 2 (DR2) of the MUSE Hubble Ultra Deep Field surveys[22]. The DR2 data consist of three datasets, a 3×3-arcmin^2 mosaic of nine MUSE fields at 10-h depth (hereafter MOSAIC), a 1×1-arcmin^2 field at 31-h depth (hereafter UDF-10) and the MUSE eXtremely Deep Field (MXDF), with a deepest achieved exposure of 141 h. This is the deepest spectroscopic survey ever performed, reaching an unresolved emission line 1σ surface-brightness limit of $<10^{-19}$ erg s^{-1} cm^{-2} arcsec^{-2}. These deep MUSE observations enable studies of extremely low surface brightnesses, such as spatially and kinematically resolved analysis of the CGM by Lyα (refs. 31–33), the detection of a cosmic web filament in Lyα emission on scales of several comoving megaparsecs (cMpc) (ref. 12).

The DR2 catalogue provides redshifts, multiband photometry, morphological and spectral properties, as well as measurements of stellar mass and star-formation rate of all the galaxies discovered in the MOSAIC, UDF-10 and MXDF fields[22,34]. In this work, we focus on the Mg II doublet. Given the wavelength range of MUSE, Mg II can be detected in the redshift interval of about 0.70–2.30. There are 568 galaxies detected in this redshift range.

As the goal of this work is to determine the azimuthal dependence of extended Mg II emission, a priori determination of galaxy orientation is required. We selected subsamples of edge-on and face-on galaxies by visual inspection. By cross-matching our visual selection with the GalPaK measurement[35] that covers a subset of this galaxy sample, we find that most of the face-on and edge-on subsamples have inclination angles of around $<30°$ and $>55°$, respectively. Even if this morphological classification is approximate, it is precise enough for our statistical analysis. To remove potentially merging objects, we exclude all pairs of galaxies with small projected angular separations (2″) and small line-of-sight relative radial velocities ($\leq$1,000 km s^{-1}). We selected 112 edge-on and 60 face-on galaxies, with accumulated exposure times of 2,599 h and 1,331 h, respectively.

The redshift and stellar mass (M_*) distributions of the parent sample and the edge-on and face-on subsamples are shown in Extended Data Fig. 1. The two subsamples are comparable with each other in redshift and mass. The median redshift is $z \approx 1.1$. The median stellar mass is approximately $10^{9.5} M_\odot$, with a $\lesssim$0.1-dex difference between the edge-on and face-on subsamples. We also note that this morphological classification is mainly reliable for galaxies with mass $M_* > 10^{8.5} M_\odot$, because lower-mass galaxies are not well resolved, even with ultra-deep HST images. The HST images of galaxies in the face-on and edge-on subsamples are presented in Extended Data Figs. 2 and 3. For the edge-on galaxies, we find the major axis for each target from the HST images by means of a principal component analysis. In Extended Data Fig. 3, we present the measurements of the galaxy major and minor axes.

Extended Mg II emission is reported in only a small number of galaxies[20]. To increase the signal-to-noise ratio (S/N), determine the average line strengths and obtain spatially resolved information on the properties of the CGM, we adopt a full three-dimensional stacking procedure. We stack the $5'' \times 5''$ MUSE mini-datacubes centred on each source. Before stacking, we remove the continuum by performing a spectral median filtering using a wide spectral window of 200 Å. This approach provides a fast and efficient way to remove continuum sources in the search for extended line emission. We also mask bright neighbouring objects to avoid possible contamination. We shifted individual datacubes and rebinned them to a common (rest-frame) wavelength frame. We did not rescale the flux of each individual datacube to correct for the impact of cosmological dimming. The cubes are averaged and weighted by the square root of their exposure time. Finally, we extract pseudo-NB images from the stacked cube.

In this work, we investigate the relation between galaxy orientation and extended Mg II emission. Therefore, for the edge-on galaxies, we stack the datacubes by realigning each one along the direction of the galaxy major axis. We then proceed with the same stacking procedure as described above using the realigned cubes. For face-on galaxies, we stack the datacubes using their original orientations.

We apply a pseudo-NB filter centred on the Mg II 2,796 Å line, with a rest-frame full width of 3 Å, corresponding to a velocity range of approximately 300 km s^{-1}. In Fig. 1, we show the first line (2,796 Å) of the Mg II doublet. An anisotropic pattern can be clearly observed around the edge-on galaxy. To quantify the statistical significance of the observed pattern, we calculate the S/N as follows. We estimate the noise by generating pseudo-NB images at 50 random wavelengths adjacent to the Mg II 2,796 Å line, within ±80 Å, while avoiding the wavelength range of the Mg II doublets. The widths of these random NBs are the same as the NB for the Mg II line. Using these random pseudo-NB images, we determine the noise and calculate the corresponding S/N. The S/N of the Mg II detection is indicated by the contours in Fig. 1. Along the minor axis of the edge-on galaxy, the anisotropic Mg II emission reaches a peak S/N of 6σ. The S/N for the face-on sample is lower but we will still show the robustness of the ring pattern in Extended Data Fig. 6.

We also plot the Mg II 2,796 Å maps at narrower velocity bins that correspond to line-of-sight velocities of $\Delta v = -150$ to -50, -50 to 50 and 50 to 150 km s^{-1} (Fig. 2). The sum of the three velocity bins corresponds to approximately 3 Å in the rest frame, so this combination of the three maps equals the pseudo-NB in Fig. 1. In Figs. 2 and 3, we calculate the S/N contours following the same method as above.

The size of the anisotropic Mg II emission
To further quantify the spatial scale of the anisotropic Mg II emission around edge-on galaxies, we measure the distance (b) of the bipolar Mg II emission to the galaxy disk. This is achieved by calculating the flux-weighted distance to the galaxy disk for the pixels within the 6σ contours in Fig. 1. The distance derived from the mean-stacked datacube is $b = 9.6 \pm 1.7$ kpc, whereas the median-stacked datacube yields a distance of $b = 9.4 \pm 2.0$ kpc. To determine the errors associated with these distances, we replicate the procedure after adding noise to produce 100 mock NB images and repeat the distance calculation.

For comparison, we also compute the size of the stellar emission region. We perform the stacking procedure on the MUSE white-light images of the edge-on galaxies, applying the same smoothing kernel as before. Subsequently, we fit a Sérsic profile to the stacked image. The resulting minor-axis effective radius is 3.2 ± 0.3 kpc.

Furthermore, we calculate the size of the anisotropic Mg II emission for the high-mass subsample in Fig. 3 using the same methodology. In this case, we use the 4σ contours to define the emission region. The distance of the bipolar Mg II emission to the galaxy disk is $b = 10.2 \pm 2.5$ kpc. We measure the minor-axis effective radius of the stellar continuum to be 3.6 ± 0.3 kpc.

Another important morphological parameter characterizing galactic outflows is the opening angle (θ). Despite the fact that galactic outflows in the local Universe do not commonly exhibit perfectly conical shapes in real observations, approximating them with an opening angle can simplify the modelling process. In this work, we are able to directly measure this parameter from the edge-on image, thanks to the preselection based on galaxy inclination. In Fig. 1, we define the extent of the outflow using a flux level that encompasses half of the peak flux ($\approx 5 \times 10^{-20}$ erg s^{-1} cm^{-2} arcsec^{-2}). For the mean and median stacks, we measure average outflow opening angles of $\theta \approx 68 \pm 8°$ and $\theta \approx 70 \pm 11°$, respectively. Similarly, using the same method, we calculate the outflow opening angle for the high-mass subsample shown in Fig. 3 to be $\theta \approx 78 \pm 15°$. It is important to note that the value of θ depends on the PSF and the smoothing kernel used, meaning that the actual θ is probably smaller than the measured value. Nonetheless, it is worth mentioning that our measurement of θ is consistent with previous absorption studies[28,36] and is also close to the opening angle measured for the nearby starburst galaxy M82 (ref. 37).

Article

The prevalence of the anisotropic Mg II emission

We have seen the anisotropic Mg II emission in both the mean and median stacks (Fig. 1), indicating that the Mg II outflows are common among the galaxies in our sample.

To further demonstrate that the stacking is not dominated by a few outliers, we perform the following analysis. We produce pseudo-NB images for each individual galaxy, using the same NB width as described above. Then we perform aperture photometry on each pseudo-NB image, placing the apertures 1″ above and below the galaxy plane along the minor axis. In this way, we measure the fluxes of the regions in which the bipolar outflows are expected. We measure the S/N of the photometry. The distribution of the surface brightness and S/N in the outflow region for the edge-on galaxy sample is shown in Extended Data Fig. 4. The smooth shape of the probability distribution indicates that the signal is not dominated by outliers. The median surface brightness of the Mg II λ2796 outflow emission is 7.9×10^{-20} erg s^{-1} cm^{-2} arcsec^{-2}. We have also tried to remove the top 5% of the edge-on galaxy sample with the highest S/N. Stacking the remaining datacubes then results in a bipolar pattern very similar to Fig. 1.

The spectroscopic properties of the extended Mg II emission

We extract the spectra from different regions in the field of view. The spectra are shown in Extended Data Fig. 5, with each panel corresponding to a grid cell at the top row in Fig. 1. The stack represents a total exposure time of thousands of hours, achieving a 1σ noise level of less than 10^{-21} erg s^{-1} cm^{-2} Å^{-1}. We see prominent signals particularly in grid cell nos. 8, 13 and 18. For edge-on galaxies, in the regions along the galaxy minor axis (for example, grid cell nos. 8 and 18), the stack shows pure emission near the systemic redshift, supporting a scenario of galactic outflow along the minor axis. The Mg II emission line doublets show a variation of line ratio over the field of view, indicating a complicated radiative-transfer process.

The centre region (for example, cell no. 13) of the edge-on sample shows a complex combination of blueshifted absorption and redshifted emission. Previous works found that Mg II spectra of galaxies seem to show pure absorption for high-mass galaxies, emission for lower-mass galaxies and P Cygni-like profiles for intermediate-mass galaxies[24].

The 'ring' pattern in the face-on galaxies

In Fig. 1 and Extended Data Fig. 5, we detect pure absorption in the centre of the stack of face-on galaxies. In the outer region, we see a weak 'ring' pattern in the NB images.

To quantify the robustness of the 'ring' pattern, we show the spectra extracted from the stacked face-on sample (red line, extracted from an annular aperture of 1″–2″) in Extended Data Fig. 6. Although the absorption is strong, the redshifted Mg II λ2796 line is evident, with S/N $\approx$ 3.2. The equivalent width (EW) of the Mg II 2,796 Å line is -21 ± 15 Å. The physical origin for this 'ring' pattern is unclear. Owing to the uncertainty in measuring the inclination angle, the face-on sample is probably not purely face-on. The 'ring' could also be attributed to inflowing or reaccreting gas or outflows extending to large radii. Further observations and simulations are needed for a better understanding.

For comparison, in Extended Data Fig. 6, we also plot spectra extracted from the bipolar outflow region (1.5″ upper and lower than the galaxy disk, with an aperture size of 1″). The EW of the Mg II 2,796 Å line is -56 ± 22 Å. Both lines of the Mg II doublet are obvious. The line ratio of the doublet is 2.3 ± 0.5, which is compatible with the value of 2 expected for an optically thin gas. The variation of the line ratio for extended Mg II emission has been reported[38]. However, with low S/N, we see variation of the Mg II doublet ratio (Extended Data Fig. 5) that may result from the complicated radiative transfer of the Mg II photons and possibly hints at the variation of gas density in an optically thin scenario[38,39].

The outflow in the down-the-barrel absorption

It is also interesting to compare the down-the-barrel spectra from the galaxies themselves. We compare the spectra extracted from the centre of the high-mass-galaxy sample in Fig. 4. The EW of the Mg II 2,796 Å line of the face-on galaxy is 7.4 ± 0.9 Å. The EW of the edge-on galaxy is 2.5 ± 0.7 Å.

The Mg II lines of the face-on galaxies are much broader than those of the edge-on galaxies, because the central spectra of the face-on galaxies contain the down-the-barrel information on the galactic outflows along the line of sight. The velocity difference of the two absorption lines thus indicates the typical velocity of the outflow (v_{out}). By measuring the Mg II λ2796 full width at half maximum difference of the face-on and edge-on galaxies, we obtain an estimate of the typical outflow velocity of 161.5 ± 27.8 km s^{-1}.

We also provide another measurement of v_{out}. We perform a two-component Gaussian fit of the Mg II λ2803 absorption line, with a Gaussian component at zero velocity and another Gaussian component with the velocity difference as a free parameter. The first Gaussian represents the Mg II from the interstellar medium of the galaxy and the second represents the galactic outflow. The fits are shown by the dotted red lines in Fig. 4. The velocity difference of the two Gaussians is 199.4 ± 19.6 km s^{-1}. Although these two estimates of the outflow velocity are crude, they are in agreement within the error range.

Physical properties of the galactic outflows

We have shown that the anisotropic Mg II emission extending up to about 10 kpc is a common phenomenon for massive edge-on galaxies at $z \approx 1$, which demonstrates the prevalence of cool and metal-enriched galactic outflows. The existence of outflows at high redshift is previously observed as the bimodal distribution of Mg II absorbers against bright background sources[25–28,40–44]. The bipolar pattern of outflows can also be statistically inferred by the down-the-barrel absorption. The strengths and kinematics of the down-the-barrel absorbers are observed as a function of galaxy-inclination angles[23,36,45,46]. At similar redshift, galactic outflows are observed individually by emission lines in several cases[17–19,47,48]. Despite these individual findings, the occurrence frequency and bipolar shape of the galactic outflows, as well as their connection to the galaxy azimuthal angle, are very unclear. In our work, Fig. 1 provides the most direct evidence of the prevalence of cool and metal-enriched galactic outflows that form a bipolar geometry. In the previous sections, by imaging the galactic outflow in spatially resolved spectroscopy, we have directly quantified its average morphology and kinematics.

Here we turn to provide an order-of-magnitude estimate of the Mg II density. This estimate is based on the Sobolev approximation[18,20,49,50]. The Sobolev approximation models the outflow with a radial-velocity gradient. Photons produced by star formation at frequency v can only be resonant when they encounter a gas parcel with velocity $v(r_s) = c(v - v_0)/v_0$. The radial-velocity gradient thus ensures that the photons can only be resonant at the Sobolev radius r_s.

In this work, we adopt the method of an identical case for an individual galaxy with Mg II emission[18]. Under the Sobolev approximation, the Mg II density can be estimated from the velocity gradient dv/dr as:

$$n_{\text{Mg}^+} \approx 6.9 \times 10^{-11} \text{ cm}^{-3} \left| \frac{dv}{dr} \frac{\text{kpc}}{\text{km s}^{-1}} \right|_{r_s} \qquad (1)$$

Considering the outflow velocity $v_{\text{out}} \approx 180$ km s^{-1}, opening angle $\theta \approx 70°$ and impact parameter $b \approx 10$ kpc, we finally get $n_{\text{Mg}^+} = 1.02 \times 10^{-9}$ cm^{-3}.

Given the ion density n_{Mg^+}, the total gas density can be estimated by correcting for metallicity $\eta(\text{Mg})$, ionization fraction $\chi(\text{Mg}^+)$ and dust depletion $d(\text{Mg})$. We assume solar metallicity, which is approximately the typical interstellar medium metallicity for similar redshift and mass range[51]. We chose a depletion typical of clouds in the Milky Way disk[18].

The ionization correction is a function of the ionization parameter, which depends on the ionizing photon luminosity Q.

$$n_H \approx 0.019 \text{ cm}^{-3}\left(\frac{n_{Mg^+}}{10^{-9} \text{ cm}^{-3}}\right)^{0.52}\left(\frac{10 \text{ kpc}}{r_s}\right)^{0.96}\left(\frac{6.3 \times 10^{-2}}{d(Mg)}\right)^{0.52}$$

$$\left(\frac{3.8 \times 10^{-5}}{\eta(Mg)}\right)^{0.52}\left(\frac{Q}{10^{53} \text{ s}^{-1}}\right)^{0.48} \quad (2)$$

Reference 22 provides measurements of the star-formation rate based on spectral-energy-distribution fitting. The median star-formation rate of our sample is about $5.1 M_\odot$ year^{-1}. We then estimate the typical Q of approximately 4.7×10^{53} s^{-1} (ref. 52). Given our input value of r_s and n_{Mg^+}, we finally get our best estimate of the hydrogen density of $n_H = 0.03$ cm^{-3}.

Finally, using the estimated H gas density and accounting for the solid angle of the outflow, we can estimate the average mass-loss rate in the cool gas traced by Mg II (ref. 18).

$$\dot{M}_{out} = 30 M_\odot \text{ year}^{-1}\left(\frac{\Omega}{\pi}\right)\left(\frac{f_c}{1}\right)\left(\frac{r}{10 \text{ kpc}}\right)^2\left(\frac{v}{180 \text{ km s}^{-1}}\right)\left(\frac{n_H}{0.03 \text{ cm}^{-3}}\right) \quad (3)$$

Here we assume the covering fraction $f_c = 1$. We finally get $\dot{M}_{out} = 36.3 M_\odot$ year^{-1}. This suggests that outflows typically remove roughly seven times more gas mass than is being converted into stars inside the galaxies at present. This roughly agrees with the predictions from simulations[53].

Note that here we only provide an order-of-magnitude estimate of $\dot{M}_{out}$. As previously mentioned, the measurements of θ and b are inevitably affected by the instrumental resolution. For our stacked face-on galaxy sample, we make the assumption that the covering fraction f_c of Mg II outflowing gas is uniformly 1. However, it is crucial to acknowledge that, in real cases, f_c may vary among different galaxies, thereby introducing nonlinear contributions to the measurements. Our estimate also depends on several parameters $\eta(Mg)$, $\chi(Mg^+)$ and $d(Mg)$, for which we do not know the exact values. For example, we may expect the typical metallicity to be subsolar. If we assume a metallicity of $0.5 Z_\odot$, then $\dot{M}_{out}$ would be boosted by a factor of 1.4. Besides these parameters, $\dot{M}_{out}$ depends mostly on v_{out}, by a power index of 1.52. To provide a possible range of $\dot{M}_{out}$, we vary v_{out} from 170 to 190 km s^{-1} and θ from 60° to 80°. In that case, $\dot{M}_{out}$ varies from 23.9 to $52.7 M_\odot$ year^{-1}.

Data availability

This work is mainly based on data release 2 (DR2) of the MUSE Hubble Ultra Deep Field surveys. The reduced MUSE datacubes are available in ref. 22.

31. Claeyssens, A. et al. Spectral variations of Lyman α emission within strongly lensed sources observed with MUSE. *Mon. Not. R. Astron. Soc.* **489**, 5022–5029 (2019).
32. Leclercq, F. et al. The MUSE Hubble Ultra Deep Field Survey. XIII. Spatially resolved spectral properties of Lyman α haloes around star-forming galaxies at z > 3. *Astron. Astrophys.* **635**, A82 (2020).
33. Erb, D. K. et al. The circumgalactic medium of extreme emission line galaxies at z~2: resolved spectroscopy and radiative transfer modeling of spatially extended Lyα emission in the KBSS-KCWI survey. *Astrophys. J.* **953**, 118 (2023).
34. Bacon, R. et al. The MUSE Hubble Ultra Deep Field Survey. I. Survey description, data reduction, and source detection. *Astron. Astrophys.* **608**, A1 (2017).
35. Bouché, N. F. et al. The MUSE Hubble Ultra Deep Field Survey. XVI. The angular momentum of low-mass star-forming galaxies: A cautionary tale and insights from TNG50. *Astron. Astrophys.* **654**, A49 (2021).
36. Rubin, K. H. R. et al. Evidence for ubiquitous collimated galactic-scale outflows along the star-forming sequence at z ~ 0.5. *Astrophys. J.* **794**, 156 (2014).
37. Walter, F., Weiss, A. & Scoville, N. Molecular gas in M82: resolving the outflow and streamers. *Astrophys. J.* **580**, L21 (2002).
38. Chisholm, J., Prochaska, J. X., Schaerer, D., Gazagnes, S. & Henry, A. Optically thin spatially resolved Mg II emission maps the escape of ionizing photons. *Mon. Not. R. Astron. Soc.* **498**, 2554–2574 (2020).
39. Katz, H. et al. Mg II in the JWST era: a probe of Lyman continuum escape?. *Mon. Not. R. Astron. Soc.* **515**, 4265–4286 (2022).
40. Bordoloi, R. et al. The radial and azimuthal profiles of Mg II absorption around 0.5 < z < 0.9 zCOSMOS galaxies of different colors, masses, and environments. *Astrophys. J.* **743**, 10 (2011).
41. Kacprzak, G. G., Churchill, C. W. & Nielsen, N. M. Tracing outflows and accretion: a bimodal azimuthal dependence of Mg II absorption. *Astrophys. J. Lett.* **760**, L7 (2012).
42. Bordoloi, R., Lilly, S. J., Kacprzak, G. G. & Churchill, C. W. Modeling the distribution of Mg II absorbers around galaxies using background galaxies and quasars. *Astrophys. J.* **784**, 108 (2014).
43. Lan, T.-W. & Mo, H. The circumgalactic medium of eBOSS emission line galaxies: signatures of galactic outflows in gas distribution and kinematics. *Astrophys. J.* **866**, 36 (2018).
44. Lundgren, B. F. et al. The geometry of cold, metal-enriched gas around galaxies at z ~ 1.2. *Astrophys. J.* **913**, 50 (2021).
45. Chen, Y.-M. et al. Absorption-line probes of the prevalence and properties of outflows in present-day star-forming galaxies. *Astrophys. J.* **140**, 445 (2010).
46. Bordoloi, R. et al. The dependence of galactic outflows on the properties and orientation of zCOSMOS galaxies at z ~ 1. *Astrophys. J.* **794**, 130 (2014).
47. Shaban, A. et al. A 30 kpc spatially extended clumpy and asymmetric galactic outflow at z ~ 1.7. *Astrophys. J.* **936**, 77 (2022).
48. Rupke, D. S. N. et al. A 100-kiloparsec wind feeding the circumgalactic medium of a massive compact galaxy. *Nature* **574**, 643–646 (2019).
49. Sobolev, V. V. *Moving Envelopes of Stars* (Harvard University Press, 1960) [transl.].
50. Carr, C., Scarlata, C., Panagia, N. & Henry, A. A Semi-analytical Line Transfer (SALT) Model. II: the effects of a bi-conical geometry. *Astrophys. J.* **860**, 143 (2018).
51. Zahid, H. J., Kewley, L. J. & Bresolin, F. The mass–metallicity and luminosity–metallicity relations from DEEP2 at z ~ 0.8. *Astrophys. J.* **730**, 137 (2011).
52. Kennicutt, R. C. Star formation in galaxies along the Hubble sequence. *Annu. Rev. Astron. Astrophys.* **36**, 189–231 (1998).
53. Mitchell, P. D. & Schaye, J. How gas flows shape the stellar–halo mass relation in the EAGLE simulation. *Mon. Not. R. Astron. Soc.* **511**, 2948–2967 (2022).

Extended Data Fig. 1 | Distribution of the redshifts and stellar masses in the MUSE sample. The parent sample is shown by grey bars and the edge-on and face-on subsamples are shown in black and red, respectively.
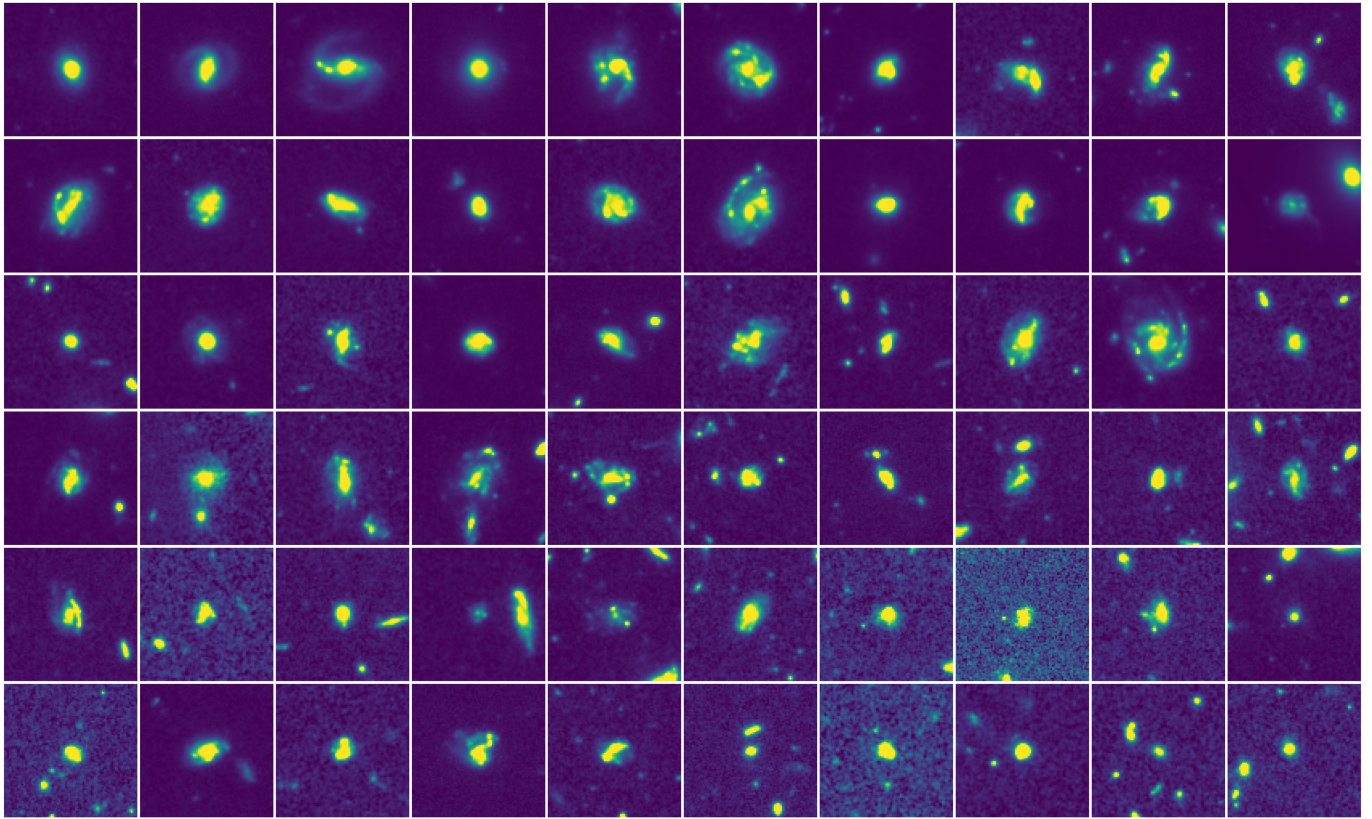
Extended Data Fig. 2 | HST images of all the face-on galaxies. Each thumbnail has the same size as in Fig. 1.
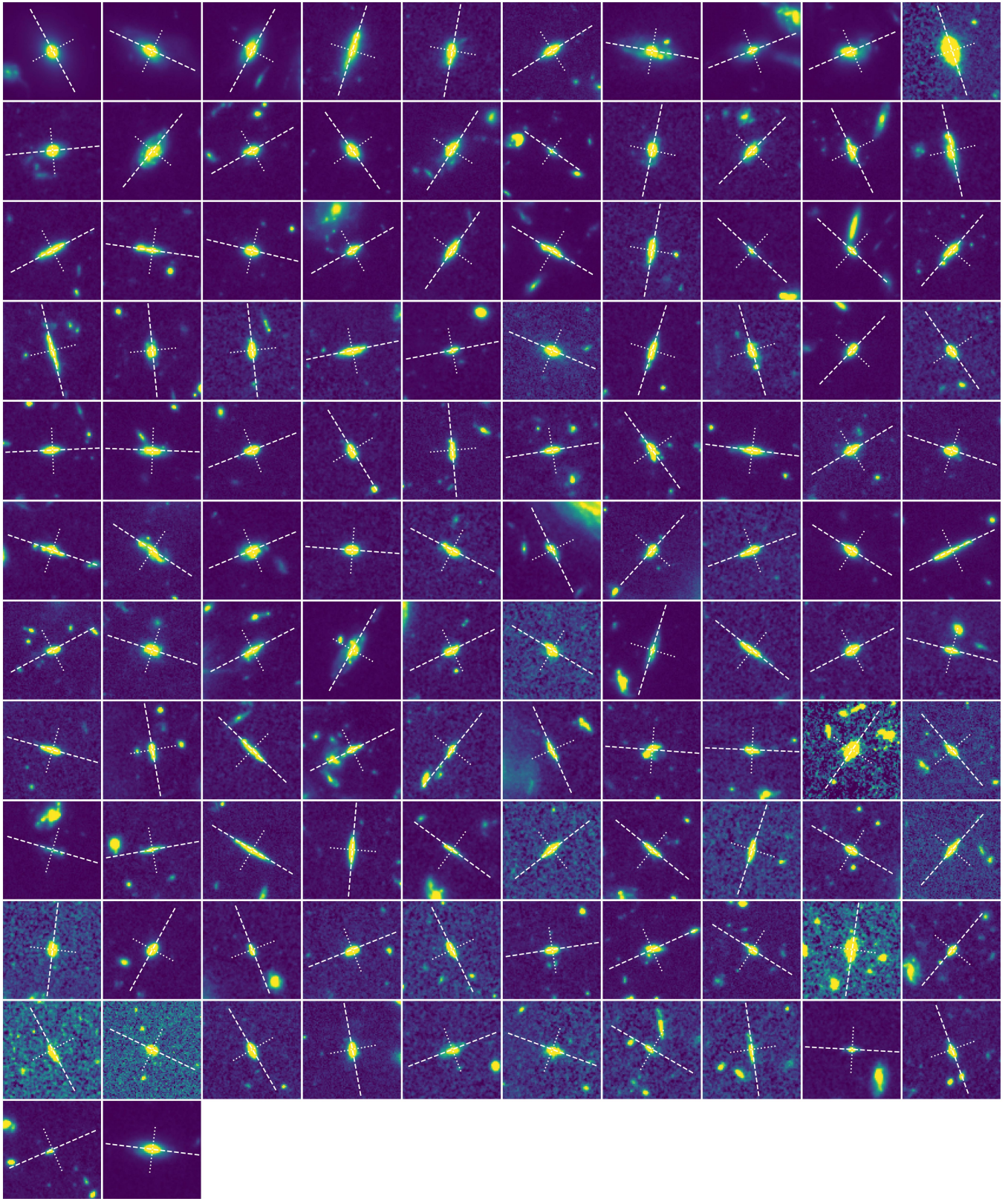
Extended Data Fig. 3 | HST images of all the edge-on galaxies. Each thumbnail has the same size as in Fig. 1. The dashed and dotted lines show the major and minor axes of the galaxies, respectively.
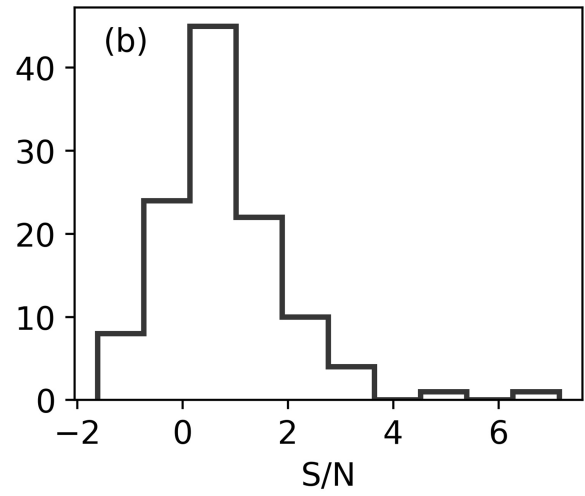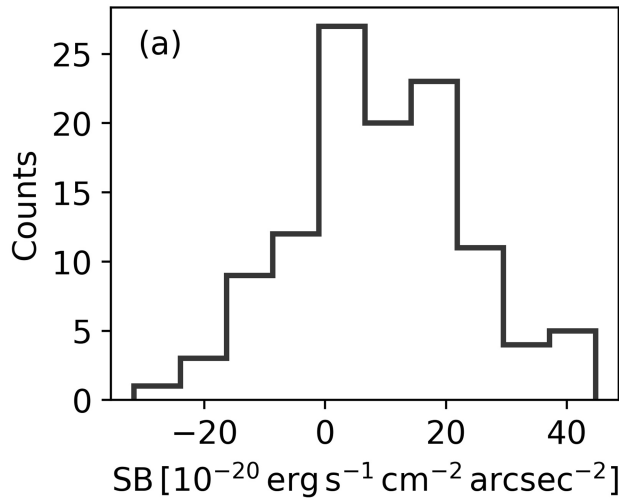
Extended Data Fig. 4 | The surface brightness of the Mg II outflow from each edge-on galaxy. The distributions of surface brightness (**a**) and S/N (**b**). The signals are extracted in 1″-diameter apertures above and below the edge-on galaxies, at a distance to the galactic plane of 1″. The distribution of surface-brightness signals skews towards positive values, despite most of the signals being of low S/N. The negative S/N values correspond to the negative signals in the left panel.
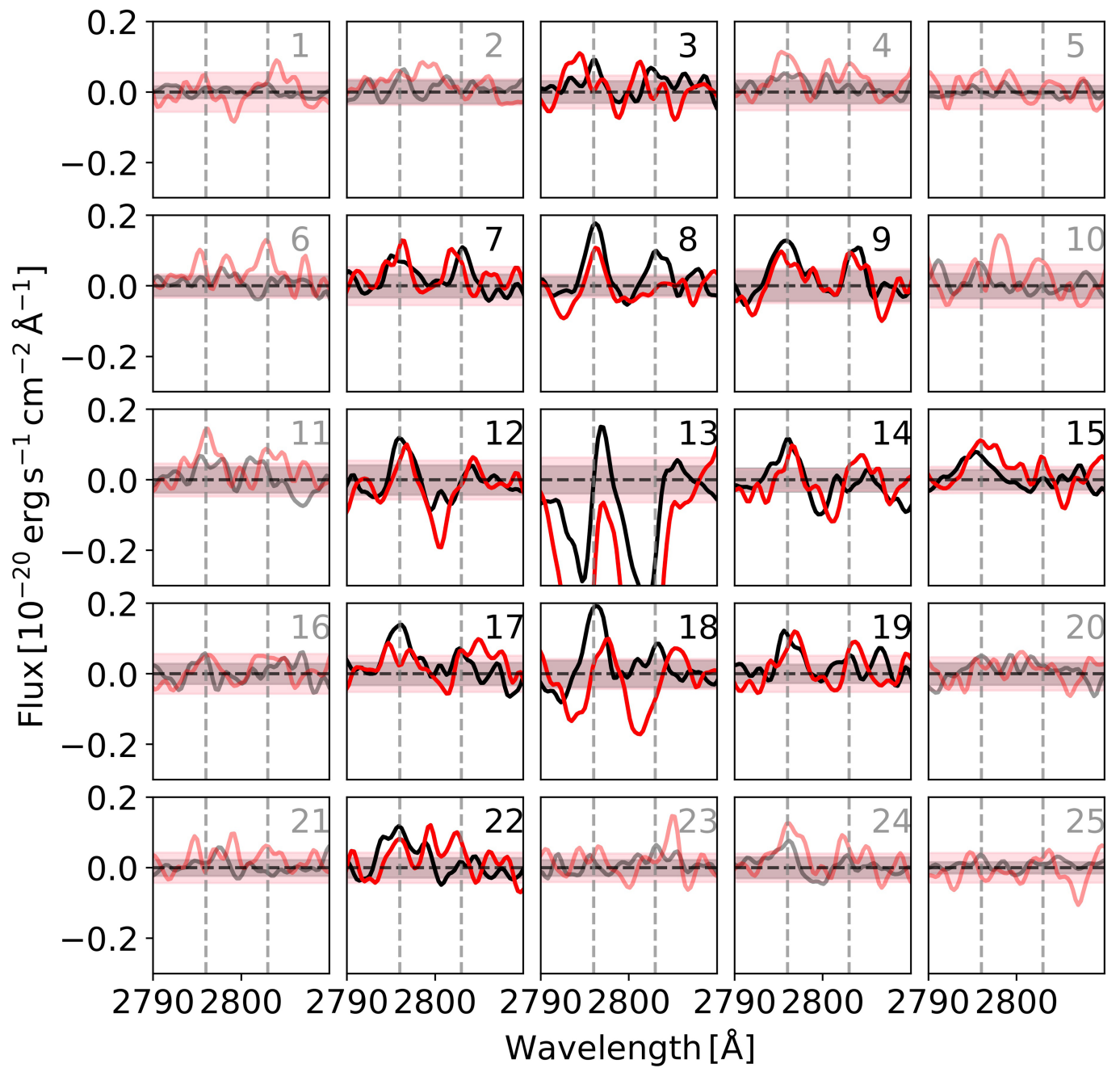
Extended Data Fig. 5 | The spectra of the extended Mg II emission. The spectra in each panel are extracted from the grid cell at the corresponding position in Fig. 1. The black and red spectra denote the edge-on and face-on galaxy samples, respectively. In each panel, the coloured shading represents the 1σ error range of the corresponding spectra. The panels for which the peak of the Mg II 2,796 Å line in the black spectra falls below the 2σ threshold are marked with a lighter colour.
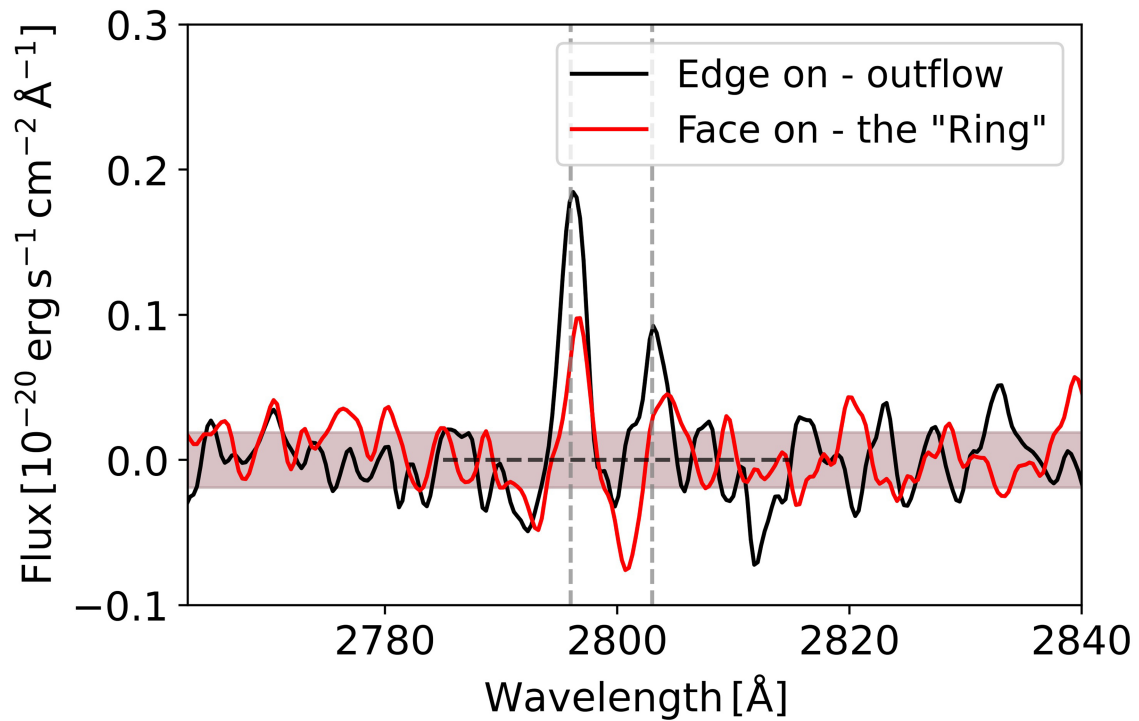
Extended Data Fig. 6 | The continuum-subtracted spectrum of the 'ring' in face-on galaxies. The red line denotes the spectrum extracted from the 'ring' region of the stacked face-on galaxy sample. For comparison, we also show the continuum-subtracted spectrum from the 'outflow' region of the edge-on galaxy. The coloured shadings represent the 1σ error range of the corresponding spectra. The two vertical dashed lines indicate the wavelength of Mg II doublets. The horizontal shadow shows the noise level. The EWs of the Mg II 2,796 Å line for the red and black spectra are -21 ± 15 Å and -56 ± 22 Å, respectively.